Assessment of systematic chromatic errors that impact sub-1% photometric precision in large-area sky surveys

Article (Published Version)

The Astronomical Journal, 151:157 (16pp), 2016 June doi:10.3847/0004-6256/151/6/157

ASSESSMENT OF SYSTEMATIC CHROMATIC ERRORS THAT IMPACT SUB-1% PHOTOMETRIC PRECISION IN LARGE-AREA SKY SURVEYS

T. S. Li[1], D. L. DePoy[1], J. L. Marshall[1], D. Tucker[2], R. Kessler[3], J. Annis[2], G. M. Bernstein[4], S. Boada[1], D. L. Burke[5,6], D. A. Finley[2], D. J. James[7], S. Kent[2], H. Lin[2], J. Marriner[2], N. Mondrik[1], D. Nagasawa[1], E. S. Rykoff[5,6], D. Scolnic[3], A. R. Walker[7], W. Wester[2], T. M. C. Abbott[7], S. Allam[2], A. Benoit-Lévy[8,9,10], E. Bertin[8,10], D. Brooks[9], D. Capozzi[11], A. Carnero Rosell[12,13], M. Carrasco Kind[14,15], J. Carretero[16,17], M. Crocce[16], C. E. Cunha[6], C. B. D'Andrea[11,18], L. N. da Costa[12,13], S. Desai[19,20], H. T. Diehl[2], P. Doel[9], B. Flaugher[2], P. Fosalba[16], J. Frieman[2,3], E. Gaztanaga[16], D. A. Goldstein[21,22], D. Gruen[5,6,2324], R. A. Gruendl[14,15], G. Gutierrez[2], K. Honscheid[25,26], K. Kuehn[27], N. Kuropatkin[2], M. A. G. Maia[12,13], P. Melchior[28], C. J. Miller[29,30], R. Miquel[17,31], J. J. Mohr[19,20,23], E. Neilsen[2], R. C. Nichol[11], B. Nord[2], R. Ogando[12,13], A. A. Plazas[32], A. K. Romer[33], A. Roodman[5,6], M. Sako[4], E. Sanchez[34], V. Scarpine[2], M. Schubnell[30], I. Sevilla-Noarbe[14,34], R. C. Smith[7], M. Soares-Santos[2], F. Sobreira[2,12], E. Suchyta[4], G. Tarle[30], D. Thomas[11], and V. Vikram[35]

(The DES Collaboration)

[1] George P. and Cynthia Woods Mitchell Institute for Fundamental Physics and Astronomy, and Department of Physics and Astronomy, Texas A&M University, College Station, TX 77843, USA
[2] Fermi National Accelerator Laboratory, P.O. Box 500, Batavia, IL 60510, USA
[3] Kavli Institute for Cosmological Physics, University of Chicago, Chicago, IL 60637, USA
[4] Department of Physics and Astronomy, University of Pennsylvania, Philadelphia, PA 19104, USA
[5] SLAC National Accelerator Laboratory, Menlo Park, CA 94025, USA
[6] Kavli Institute for Particle Astrophysics & Cosmology, P.O. Box 2450, Stanford University, Stanford, CA 94305, USA
[7] Cerro Tololo Inter-American Observatory, National Optical Astronomy Observatory, Casilla 603, La Serena, Chile
[8] CNRS, UMR 7095, Institut d'Astrophysique de Paris, F-75014, Paris, France
[9] Department of Physics & Astronomy, University College London, Gower Street, London, WC1E 6BT, UK
[10] Sorbonne Universités, UPMC Univ Paris 06, UMR 7095, Institut d'Astrophysique de Paris, F-75014, Paris, France
[11] Institute of Cosmology & Gravitation, University of Portsmouth, Portsmouth, PO1 3FX, UK
[12] Laboratório Interinstitucional de e-Astronomia—LIneA, Rua Gal. José Cristino 77, Rio de Janeiro, RJ—20921-400, Brazil
[13] Observatório Nacional, Rua Gal. José Cristino 77, Rio de Janeiro, RJ—20921-400, Brazil
[14] Department of Astronomy, University of Illinois, 1002 W. Green Street, Urbana, IL 61801, USA
[15] National Center for Supercomputing Applications, 1205 West Clark Street, Urbana, IL 61801, USA
[16] Institut de Ciències de l'Espai, IEEC-CSIC, Campus UAB, Carrer de Can Magrans, s/n, E-08193 Bellaterra, Barcelona, Spain
[17] Institut de Física d'Altes Energies (IFAE), The Barcelona Institute of Science and Technology, Campus UAB, E-08193 Bellaterra (Barcelona) Spain
[18] School of Physics and Astronomy, University of Southampton, Southampton, SO17 1BJ, UK
[19] Excellence Cluster universe, Boltzmannstrasse 2, D-85748 Garching, Germany
[20] Faculty of Physics, Ludwig-Maximilians University, Scheinerstrasse 1, D-81679 Munich, Germany
[21] Department of Astronomy, University of California, Berkeley, 501 Campbell Hall, Berkeley, CA 94720, USA
[22] Lawrence Berkeley National Laboratory, 1 Cyclotron Road, Berkeley, CA 94720, USA
[23] Max Planck Institute for Extraterrestrial Physics, Giessenbachstrasse, D-85748 Garching, Germany
[24] Universitäts-Sternwarte, Fakultät für Physik, Ludwig-Maximilians Universität München, Scheinerstrasse 1, D-81679 München, Germany
[25] Center for Cosmology and Astro-Particle Physics, The Ohio State University, Columbus, OH 43210, USA
[26] Department of Physics, The Ohio State University, Columbus, OH 43210, USA
[27] Australian Astronomical Observatory, North Ryde, NSW 2113, Australia
[28] Department of Astrophysical Sciences, Princeton University, Peyton Hall, Princeton, NJ 08544, USA
[29] Department of Astronomy, University of Michigan, Ann Arbor, MI 48109, USA
[30] Department of Physics, University of Michigan, Ann Arbor, MI 48109, USA
[31] Institució Catalana de Recerca i Estudis Avançats, E-08010 Barcelona, Spain
[32] Jet Propulsion Laboratory, California Institute of Technology, 4800 Oak Grove Drive, Pasadena, CA 91109, USA
[33] Department of Physics and Astronomy, Pevensey Building, University of Sussex, Brighton, BN1 9QH, UK
[34] Centro de Investigaciones Energéticas, Medioambientales y Tecnológicas (CIEMAT), Madrid, Spain
[35] Argonne National Laboratory, 9700 South Cass Avenue, Lemont, IL 60439, USA

Received 2016 January 1; accepted 2016 March 14; published 2016 May 27

ABSTRACT

Meeting the science goals for many current and future ground-based optical large-area sky surveys requires that the calibrated broadband photometry is both stable in time and uniform over the sky to 1% precision or better. Past and current surveys have achieved photometric precision of 1%–2% by calibrating the survey's stellar photometry with repeated measurements of a large number of stars observed in multiple epochs. The calibration techniques employed by these surveys only consider the relative frame-by-frame photometric zeropoint offset and the focal plane position-dependent illumination corrections, which are independent of the source color. However, variations in the wavelength dependence of the atmospheric transmission and the instrumental throughput induce source color-dependent systematic errors. These systematic errors must also be considered to achieve the most precise photometric measurements. In this paper, we examine such systematic chromatic errors (SCEs) using photometry from the Dark Energy Survey (DES) as an example. We first define a natural magnitude system for DES and calculate the systematic errors on stellar magnitudes when the atmospheric transmission and instrumental throughput deviate from the natural system. We conclude that the SCEs caused by the change of airmass in each exposure, the change of the precipitable water vapor and aerosol in the atmosphere over time, and the non-

uniformity of instrumental throughput over the focal plane can be up to 2% in some bandpasses. We then compare the calculated SCEs with the observed DES data. For the test sample data, we correct these errors using measurements of the atmospheric transmission and instrumental throughput from auxiliary calibration systems. The residual after correction is less than 0.3%. Moreover, we calculate such SCEs for Type Ia supernovae and elliptical galaxies and find that the chromatic errors for non-stellar objects are redshift-dependent and can be larger than those for stars at certain redshifts.

Key words: atmospheric effects – methods: observational – surveys – techniques: photometric

1. INTRODUCTION

In traditional astronomical photometry, a set of standard stars, such as those from Landolt's (Landolt 1992) or Stetson's (Stetson 2000, 2005) catalogs, is observed over a wide range of airmasses during the course of a night to calibrate all of the sources observed on the same night. The observed instrumental magnitude m_b and the standard magnitude m_b^0 for a given bandpass b have the following relation:

$$m_b - m_b^0 = a_b + k_b \cdot X + c_b \cdot \mathrm{color}, \quad (1)$$

where a_b is the photometric zeropoint, k_b is the first-order atmospheric extinction coefficient, X is the airmass for each exposure, c_b is the color term coefficient, and *color* is the color of the stars (e.g., $g - r$ or $V - R$, depending on the photometric systems and the filter bandpasses). On a photometric night—i.e., a night in which the atmospheric extinction coefficient is stable over time and uniform over the sky—the nightly a_b and k_b are derived. The color term c_b is a first-order correction to compensate for the difference in the *shape* of the filter bandpass of the standard system and that of the filter bandpass actually used in the night's observations. This term corrects for the full system response for that filter bandpass, including both the instrument throughput and the atmospheric transmission. Fortunately, for most optical passbands, the color term coefficients are reasonably constant over the course of a typical observing run ($\lesssim$1 week), and by fitting the above relation to observations of standard stars and applying the results to the science exposures, all of the program target objects can be calibrated to a standard photometric system with reasonable precision.

We note that tying data to a standard system serves two aspects of photometric calibration: *relative* calibration and *absolute* calibration. Relative calibration refers to creating a data set whose photometry is internally consistent: e.g., the measured brightness and color of a (non-variable) star is, all else being equal, independent of its time of observation or its location on the sky. Absolute calibration refers to creating a data set whose photometry can be tied to physical units of specific flux (see e.g., Scolnic et al. 2015, for a review). By tying data to a standard system, one ensures that the data are consistent with the standard photometric system and can connect the apparent brightnesses and colors of stars in one's own data to those of stars that have calibrated magnitudes that are convertible to units of specific flux in erg s^{-1} cm^{-2} Hz^{-1} (Holberg & Bergeron 2006).

In recent years, large imaging surveys like the Sloan Digital Sky Survey (SDSS) have opted to create their own standard photometric systems—ones based on the "natural" photometric system of their instruments[36]—rather than try to transform their immense quantities of data to a previously defined standard system, like the Johnson-Cousins $UBVR_{\mathrm{cIc}}$ system (Bessell 1990; Bessell & Murphy 2012). A practical advantage of this is that it effectively decouples the photometric calibration of data taken in one filter with data taken in another filter: in other words, one need not match data from one filter to data in another filter in order to apply a color term, and this works sufficiently well for calibrating large optical imaging surveys at the ~2% (0.02 mag) level.

With the success of these earlier surveys, photometric calibration has become an important factor in the systematic error budgets in the era of precision cosmology. Therefore, many current and future ground-based wide-field imaging surveys have the ambitious calibration goal of "breaking the 1% barrier," which requires that calibrated broadband photometry is both stable in time and uniform over the sky to <1% (0.01 mag or 10 millimag) rms precision. These sub–1% precision requirements are driven by the specific science needs of photometric redshift accuracy, the separation of stellar populations, detection of low-amplitude variable objects, and the search for systematic effects in Type Ia supernova (SN Ia) light curves (see more details e.g., in the Large Synoptic Survey Telescope Science Book, LSST Science Collaboration et al. 2009).

Traditionally, photometry with ~1% level precision is reachable when careful analysis is taken on the flat fielding, such as star flats (Manfroid 1995), across a small field of view (FOV), and when observations are done under photometric conditions, i.e., atmospheric conditions are stable and free of clouds. Thanks to the continuous and rapid observing cadence of these dedicated surveys, overlapping areas with multi-epoch observations can be used to calibrate the illumination pattern of the imaging system with a large FOV. Indeed, Padmanabhan et al. (2008) applied the "Ubercal" procedure to the SDSS data taken in good photometric conditions and reached rms of 1%–2% relative photometry. Many other sky surveys, such as Pan-STARRS (Schlafly et al. 2012) and Deep Lens Survey (Wittman et al. 2012) have also adopted this calibration procedure for their photometric calibrations.

In order to maximize survey efficiency, imaging surveys might also be conducted in less than ideal conditions, i.e., cloudy or partly cloudy nights. Again, owing to the overlapping area in multi-epoch observations, the repeated measurements of a large number of stars allow an internal global calibration of the frame-to-frame zeropoint offset (Glazebrook et al. 1994), which links the instrumental magnitude and natural magnitude of the survey. This zeropoint offset can be a combination of the instrumental zeropoint change, the atmospheric extinction at a given airmass, and

[36] A natural system is one in which the color term coefficients c_b are all identically zero. Since system responses can and do change with time or even spatially across a survey instrument's field of view, surveys tend to *define* their natural systems by their instrument's mean system response, thus ensuring any color terms are very small and average to zero.

cloud extinction. One zeropoint offset is computed and applied to each exposure or each CCD detector, depending on the airmass of the exposure as well as photometric condition. For example, when the airmass is small and the night is photometric, the zeropoint offset could be computed on an exposure-by-exposure level; when the airmass is large or the night is cloudy, then the zeropoint offset could be computed on a CCD-by-CCD level. MacDonald et al. (2004) used this technique on the global calibration of Oxford-Dartmouth Thirty Degree Survey.

The Dark Energy Survey (DES) is a wide-area photometric survey of 5000 square degrees using the Dark Energy Camera (DECam) at the Cerro Tololo Inter-American Observatory (CTIO) 4 m Blanco telescope. DECam is composed of 74 250 μm thick fully depleted CCDs—62 for science imaging, plus 12 CCDs for real-time guiding and focus—with a FOV of $2.^{\circ}2$ (3.1 deg^2 in area) and a pixel scale of 0.26 arcsec/pixel. The filters are 620 mm in diameter and fully cover the 62 science CCDs. For further details on DECam itself, see Flaugher et al. (2015). DES has a requirement for relative photometric calibrations: the survey calibrations must be internally consistent both spatially over the survey footprint and temporally over the 5 years of the survey to at least 2% with a goal of 1% or better. However, one of its four main probes of cosmological parameters—the Hubble Diagram of Type Ia supernovae (SNe Ia)—requires photometric precision better than 1% for the 10 supernova fields. To achieve these relative calibration requirements, DES uses a combination of calibration methods mentioned above. First, star flats are obtained at the beginning of each DES season and during engineering nights in order to obtain robust pupil ghost and illumination corrections for the flat-fielding exposures (G. Bernstein et al. 2016, in preparation). Second, over its 5 year run, DES will cover its full footprint 10 times (in 10 "tilings") in each of its 5 filters (DES-*grizY*[37]), and it uses the large overlaps between exposures in different tilings to tie together the relative calibrations globally across the full survey footprint. Meanwhile, a sparse grid-work of stars extracted from the multiple DES tilings and calibrated via nightly DES standard star solutions serves both to "anchor" the relative calibrations against large-scale (but low-amplitude) systematic gradients that are often inherent to Ubercal techniques and to tie the relative calibrations to an absolute flux calibration (Tucker et al. 2007; D. L. Tucker et al. 2016, in preparation).

However, most of the calibration techniques discussed above consider only the relative frame-by-frame zeropoint offset and position dependent illumination corrections, which are independent of the source color, i.e., grayscale zeropoint corrections, or gray-term. In reality, variations in the wavelength dependence of the system response (i.e., atmospheric transmission + instrumental throughput) can also induce changes in measuring the brightness of an object that depend on the spectral energy distributions (SEDs) of the object. We refer to such changes as systematic chromatic errors, or SCEs, throughout this paper. We use the word "chromatic," since this effect could be considered as approximately linear to stellar colors, which is similar to a linear color-term correction (e.g., c_b in Equation (1)) used to transform from one photometric system to another. It is essentially the change of the *shape* of the system response. At 1% level photometric precision, SCEs are significant components of the total photometric error budget when calibration techniques only include grayscale zeropoint corrections. In a few previous imaging surveys, SCEs have been partially considered. For example, Ivezić et al. (2007) applied color-term corrections for different transmission curves from six camera columns when making the SDSS standard star catalog for Stripe 82. The Supernova Legacy Survey (SNLS) built a photometric response map to correct the non-negligible color-term variations between photometric measurements obtained at different focal plane positions of the wide field imager MegaCam (Regnault et al. 2009). Betoule et al. (2013) also considered such color-term variations in a combined photometric calibration of the SNLS and the SDSS supernova survey. Most past surveys, however, did not include corrections for SCEs in their photometric calibration, especially the SCEs from the atmospheric variation, as these corrections are small and hard to determine using the data alone. In this paper, we calculate the SCEs and show that these errors are caused by not only the non-uniformity of system response function over the focal plane, but also the change of airmass in each exposure and the change of the precipitable water vapor (PWV) and aerosol in the atmosphere over time. We also demonstrate that our calculations match what we observe in the DES data.

This paper will only discuss the photometric calibrations from the detectors to the top of Earth's atmosphere. It is worth noting that Galactic interstellar extinction is also a very important aspect in order to achieve sub-1% photometric precision, as the reddening will affect the color of objects measured at the top of the Earth atmosphere. Photometric calibration performed using the stellar locus regression technique (Ivezić et al. 2004; MacDonald et al. 2004; High et al. 2009) corrects the zeropoint variation caused by Galactic extinction. Recently, Yuan et al. (2015) used a spectroscopy-based stellar color regression method to reanalyze the SDSS data with spectra obtained from the LAMOST survey (Deng et al. 2012) and delivered an accuracy of a few millimag for color calibration. It is true that interstellar extinction will complicate the uniformity of the zeropoint calibration across the sky. However, the effect of interstellar extinction is somewhat different from the SCEs discussed in this paper, since at any given line of sight the reddening is constant and should not change the color of objects in repeated observations.

We structure the paper as follows: in Section 2, we discuss possible variations in the system response and define a fiducial system response for the DES natural system. In Section 3, we calculate the synthetic SCEs for stellar objects when the system response deviates from a fiducial system response. In Section 4, we compare these synthetic SCEs with actual DES data and show the SCEs could be corrected using the synthetic SCEs when the actual atmospheric transmission and instrumental throughput are measured directly. We then calculate the synthetic SCEs for non-stellar objects, e.g., SNe Ia and galaxies, at different redshifts in Section 5. Section 6 gives a discussion about the possible SCEs in ground-based differential photometric transit observations, followed by the conclusions in Section 7.

[37] DECam has seven filters. They are DECam-*u*, DES-*g*, DES-*r*, DES-*i*, DES-*z*, DES-*Y*, and DECam-*VR*. DES has no *u*-band component in its primary survey. However, we include discussion of DECam-*u* in this paper since it is available for all DECam community users. For simplicity, we will refer to the six bands as *ugrizY* in the paper.

2. VARIATION IN THE SYSTEM RESPONSE

Given a specific flux of an object at the top of the atmosphere, $F_\nu(\lambda)$, the total ADU counts F that are measured by a camera with a photon detector (e.g., Charge Coupled Device, or CCD) can be calculated as

$$F = C\int_0^\infty F_\nu(\lambda)S_b(\lambda)\lambda^{-1}d\lambda. \quad (2)$$

Here, $S_b(\lambda)$ is the system response function for a given bandpass b. The system response includes the Earth's atmospheric transmission along the line of sight, the reflectivity of the mirrors on the telescope, the transmission of the camera lenses and filters, and the quantum efficiency of the detector. C is a constant and is related to the effective collecting area of the primary mirror A, the inverse gain of the CCD g (electron/ADU), and the exposure time Δt:

$$C \propto \frac{A\Delta t}{g}. \quad (3)$$

The constant C is not strictly necessary for the calibration, as the observations of spectrophotometric standards (such as DA white dwarfs) using the same instrument can tie a specific natural system onto an AB magnitude system without knowing the actual value of C.

Stubbs & Tonry (2006) proposed that the process of photometric calibration can be separated into the measurement of the atmospheric transmission and a measurement of the instrumental throughput, so that the system response could be separated as

$$S_b(\lambda) = S^{\rm atm}(\lambda) \times S_b^{\rm inst}(\lambda). \quad (4)$$

The atmospheric transmission $S^{\rm atm}(\lambda, alt, az, t)$ could change over time and could also depend on the position of the object in the sky (alt, az). It may vary in both a grayscale (wavelength-independent) and a non grayscale (wavelength-dependent or the *shape* of the transmission curve) manner. Studies have shown that the atmosphere, especially the PWV, is homogeneous across the sky (Li et al. 2014; Querel & Kerber 2014); we therefore do not discuss the spatial variation of atmospheric conditions in the rest of the paper.

The instrumental throughput $S_b^{\rm inst}(\lambda, x, y, t)$ is similar, except that it may vary over time as well as over the position (x, y) on the detector focal plane. Again, the throughput can also vary in both a grayscale and a non grayscale manner. It is therefore convenient to separate the system response into a wavelength-independent normalization factor N and a wavelength-dependent *shape* factor $\phi(\lambda)$[38] for each bandpass b:

$$S_b(\lambda) = N_{\rm atm} \times \phi^{\rm atm}(\lambda) \times N_{\rm inst}^b \times \phi_b^{\rm inst}(\lambda). \quad (5)$$

Equation (2) then can be rewritten as

$$F = C \times N_{\rm atm} \times N_{\rm inst}^b \int_0^\infty F_\nu(\lambda)\phi^{\rm atm}(\lambda)\phi_b^{\rm inst}(\lambda)\lambda^{-1}d\lambda. \quad (6)$$

Over a wide area imaging survey that might be conducted for months or years, both N and $\phi(\lambda)$ could be slightly different from one exposure to another, or even within one exposure. For example, airmass extinction and clouds affect $N_{\rm atm}$; dust on the mirror affects $N_{\rm inst}$. As described in Section 1, multiple tilings of the survey area, with the repeated measurements of a large number of stars, allow the monitoring of the zeropoint offsets over time and the illumination correction over the focal plane. This paper will not discuss the calibration for the grayscale variation, i.e., variation of N, as the grayscale correction procedure mentioned in Section 1 is adequate to calibrate those variations. In this paper we will focus on the variation of the *shape* of the system response (i.e., atmospheric transmission + instrumental throughput), $\phi_b(\lambda) = \phi^{\rm atm}(\lambda, t) \times \phi_b^{\rm inst}(\lambda, x, y, t)$. The variation of ϕ_b will essentially induce the SCEs.

2.1. Variation in the Atmospheric Transmission ϕ^{atm}

Atmospheric transmission in the wavelength range covered by DES (300 nm–1100 nm) is mainly determined by the following four processes in the Earth's atmosphere (Stubbs et al. 2007): Rayleigh scattering from molecules, aerosol scattering from small particles, molecular absorption, in particular by O_2, O_3, and H_2O, and cloud extinction. The size of water droplets and ice crystals that make up clouds are larger than the wavelength of visible light, and the attenuation by clouds is wavelength independent (Ivezić et al. 2007; Burke et al. 2014; Li et al. 2014). Cloud extinction is therefore calibrated with grayscale corrections so we do not consider it in this paper.

The cross-sections of Rayleigh scattering and aerosol scattering both vary smoothly with the wavelength of the incident light. The optical depth of Rayleigh scattering has a wavelength dependence of λ^{-4} (Rayleigh 1899). At zenith, it can be simply scaled with the barometric pressure P_0 (Hansen & Travis 1974).

The optical depth of aerosol scattering at zenith could be approximately described by the Ångström formula (Ångström 1924):

$$\tau_{\rm aerosol} = \tau_0\left(\frac{\lambda}{\lambda_0}\right)^{-\alpha}, \quad (7)$$

where τ_0 is the aerosol optical depth at reference wavelength λ_0, where $\lambda_0 = 550$ nm is a convenient reference wavelength. The Ångström exponent α is inversely related to the average size of the particles in the aerosol: the smaller the particles, the larger the exponent. In general, α ranges from 0 to 3 with typical values around 1 to 1.3, depending on the geographic location. $\alpha < 1$ indicates size distributions dominated by coarse mode aerosol that are usually associated with dust and sea salt, and $\alpha > 2$ indicates size distributions dominated by fine mode aerosols that are usually associated with urban pollution and biomass burning (Schuster et al. 2006). $\alpha = 0$ and $\alpha = 4$ are essentially the two extreme cases of cloud extinction and Rayleigh scattering.

Absorption by molecules only occurs at specific wavelengths. The strong absorption lines by O_2 at 690 nm and 760 nm (Fraunhofer "B" and "A" bands) are saturated and are closely proportional to the square root of the barometric pressure, so they can be computed and scaled with Rayleigh scattering (Burke et al. 2010). O_3 absorption mainly affects atmospheric transmission shortwards of 350 nm and in the Chappuis band (450–700 nm). The optical depth of ozone scales with the ozone column density. Ozone column density is

[38] Here, $\phi(\lambda)$ is a scaleless function, i.e., only the *shape* matters. For simplicity, we can define it as $\phi_b(\lambda) = \frac{S_b(\lambda)}{\int S_b(\lambda)d\lambda}$ and $N = \int S_b(\lambda)d\lambda$. This definition is different from Ivezić et al. (2007), where they defined $\phi_b(\lambda) = \frac{\lambda^{-1}S_b(\lambda)}{\int \lambda^{-1}S_b(\lambda)d\lambda}$. Our definition of $\phi(\lambda)$ represents what we measure from the auxiliary calibration systems, and thus does not include the λ^{-1} factor.

Table 1
Synthetic SCEs on a M6V Star ($g - i \sim 4$) with Respect to a G2V Star ($g - i \sim 0.6$)

Component	Fiducial	Changed[a]	Synthetic SCEs (mmag)					
			u	g	r	i	z	Y
Pressure	$P_0 = 779$ hpa	$P_0 = 789$ hpa	−0.2	−0.4	−0.08	−0.06	0.04	−0.02
Aerosol	$\mathrm{AOD}_{550} = 0.02$, $\alpha = 1$	$\mathrm{AOD}_{550} = 0.20$, $\alpha = 1$	−3	−11	−6	−4	−1	−0.2
	$\mathrm{AOD}_{550} = 0.02$, $\alpha = 1$	$\mathrm{AOD}_{550} = 0.20$, $\alpha = 0.5$	−41	−5	−3	−2	−0.8	−0.1
PWV	PWV = 3 mm	PWV = 10 mm	0	0	3	−0.6	+10	−3
Ozone	Ozone = 270 DU	Ozone = 230 DU	0	−0.7	0.9	0.1	0	0
Airmass	$X = 1.2$	$X = 1.8$	−9	−13	−6	−2	+2	−0.8
Instrument	DECal scan	shift 2 nm	−24	−15	−16	−19	−10	−5

Note.
[a] The "changed" conditions here are just examples. For pressure and ozone, we used the extreme examples since the SCEs are small; for aerosol, PWV, and airmass, we give the examples where the change could introduce about 1% or 10 mmag SCEs. For the instrument, we choose the 2 nm shift as it is about the average value from the DECal scans.

usually measured in Dobson units (DU). Each Dobson unit is equivalent to a thickness of 0.01 mm of ozone at standard temperature and pressure. H_2O absorption mainly influences the atmospheric transmission at wavelengths longer than 600 nm. The optical depth can be scaled with the PWV column density in millimeters.

Both the optical depth and the column density mentioned correspond to the vertical path from the observer's location to the top of Earth's atmosphere. For a given atmospheric condition, the atmospheric transmission T of the light also depends on the airmass of the observation. For molecular and aerosol scattering, the transmission T at airmass $X = 1$ and at airmass $X = n$ has the following simple relation:

$$T(\lambda, X = n) = T^n(\lambda, X = 1). \quad (8)$$

The transmission due to molecular absorption, however, has a nonlinear curve of growth with respect to the optical depth or the airmass because the absorption departs from the optically thin limit.

We conclude here that the following six parameters determine a specific *shape* of the atmospheric transmission $\phi^{\mathrm{atm}}(\lambda)$: (1) airmass X of the observation, (2) barometric pressure P_0, (3) aerosol optical depth at 550 nm AOD_{550}, (4) Ångström exponent α, (5) ozone column density *Ozone*, and (6) PWV column density PWV. We define the six parameters for a fiducial atmospheric transmission curve at CTIO using $X = 1.2$, $P_0 = 779$ hpa (1 hpa = 100 pascal), Ozone column density = 270 DU, PWV = 3 mm, $\mathrm{AOD}_{550} = 0.02$, and $\alpha = 1$, which are also listed in Table 1. We choose an airmass of 1.2 as one that is typical of observations in DES wide-field survey. Meteorology data from CTIO show that the average barometric pressure during the year 2014 was 779 hpa with standard deviation of 3 hpa. Ozone column density at CTIO ranged from 240 DU to 300 DU with a mean of roughly 270 DU in 2014 according to the NASA Ozone Mapping and Profiler Suite (OMPS) Nadir Mapper.[39] CTIO does not have instrumentation to examine PWV, AOD and α. DES therefore deployed the Atmospheric Transmission Monitoring Camera (aTmCam, Li et al. 2012, 2014) in the summer of 2014, preceded by prototype tests in 2012 October–November and 2013 September–October, to study the water vapor and aerosol at CTIO. aTmCam is a robotic multi-band imaging system. During DES observations, aTmCam takes simultaneous images in four narrow (∼10 nm) bands centered at 394 nm, 520 nm, 854 nm, and 940 nm. The aTmCam analysis derives the parameters of the atmospheric transmission models at CTIO including PWV and AOD.[40] PWV = 3 mm and $\mathrm{AOD}_{550} = 0.02$ were the average values at CTIO from those early results. The long-term variation range of PWV and AOD at CTIO is not yet clear, but preliminary aTmCam results indicate that PWV varies in the range 0–20 mm and AOD varies in the range 0–0.2. Using the aforementioned parameters, we generated the fiducial atmospheric transmission

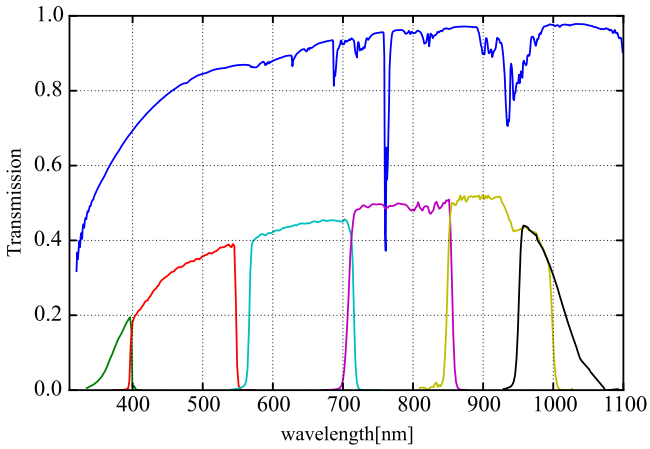

Figure 1. Fiducial atmospheric transmission $\phi^{\mathrm{atm}}_{\mathrm{ref}}(\lambda)$ at CTIO (upper curve) and the fiducial instrumental throughput $\phi^{\mathrm{inst}}_{b,\mathrm{ref}}(\lambda)$ of the DES-*ugrizY* filter bandpasses (lower curves). As DECal only provides a relative throughput measurement, the scale of the lower curves is arbitrary to provide a better visualization.

[39] http://ozoneaq.gsfc.nasa.gov/tools/ozonemap/

[40] For more information, please see the cited papers or visit http://instrumentation.tamu.edu/aTmCam.html.

$\phi_{\rm ref}^{\rm atm}(\lambda)$ using *libRadTran*[41] (Mayer & Kylling 2005), as shown in Figure 1.

2.2. Variation in the Instrumental Throughput $\phi_b^{\rm inst}$

Instrumental throughput is a combination of the mirror reflectivity, lens transmission, filter transmission, and detector sensitivity. The *shape* of the throughput may vary over time as the detector temperature changes or the filter coatings age. It may also have a spatially dependent variation over the focal plane. Furthermore, each CCD has its own response function. DES has deployed a spectrophotometric calibration system (DECal) that scans the instrument response for all bandpasses by measuring the relative instrumental throughput as a function of wavelength (Rheault et al. 2012). DECal is used to scan the wavelength range of each filter several times a year, typically during cloudy nights, to monitor the instrumental throughput over time. DECal measurements indicate that the filter bandpass edges vary with focal plane position, primarily with radial position and in the i band in particular. This effect is largely due to slightly inhomogeneous filter transmission with incident angle. Here, we define the fiducial instrumental throughput $\phi_{\rm ref}^{\rm inst}(\lambda)$ from the results of DECal scans obtained during 2013 September–November. We use the average throughput over the entire focal plane as the fiducial instrumental throughput, which is also shown in Figure 1.

3. SYNTHETIC SCES

In this section, we calculate the synthetic SCEs when the atmospheric transmission $\phi^{\rm atm}(\lambda)$ and the instrumental throughput $\phi^{\rm inst}(\lambda)$ deviate from the fiducial values defined in Section 2. We define the synthetic SCEs, Δm, as

$$\Delta m = -2.5\log_{10}\frac{\int_0^\infty F_\nu(\lambda)\phi^{\rm atm}(\lambda)\phi_b^{\rm inst}(\lambda)\lambda^{-1}d\lambda}{\int_0^\infty F_\nu(\lambda)\phi_{\rm ref}^{\rm atm}(\lambda)\phi_{b,\rm ref}^{\rm inst}(\lambda)\lambda^{-1}d\lambda} + 2.5\log_{10}\frac{\int_0^\infty F_\nu^{\rm ref}(\lambda)\phi^{\rm atm}(\lambda)\phi_b^{\rm inst}(\lambda)\lambda^{-1}d\lambda}{\int_0^\infty F_\nu^{\rm ref}(\lambda)\phi_{\rm ref}^{\rm atm}(\lambda)\phi_{b,\rm ref}^{\rm inst}(\lambda)\lambda^{-1}d\lambda}. \quad (9)$$

The first term is the change in magnitude for an object with SED $F_\nu(\lambda)$ when $\phi^{\rm atm}$ and/or $\phi_b^{\rm inst}$ deviate from fidicual values. We use the SEDs of main-sequence stars O5V-M6V from the Pickles Atlas (Pickles 1992) as $F_\nu(\lambda)$ for this calculation. The second term is the change in magnitude for a reference star. $\Delta m = 0$ when the SED of the object is the same as the reference star. This reference star plays a similar role that calibration stars play in the zeropoint computation from the global calibration or the illumination correction in the calibration procedure of DES. The only difference is that the actual survey calibration stars have a range of colors, and the gray-term correction is derived for the average color of the calibration stars. We pick a solar-type (G2V; $g-i\sim0.6$) star as the reference star, i.e., a G2V star will have zero Δm due to the change of atmospheric transmission and/or instrumental throughput.

[41] libRadTran is a collection of C and Fortran functions and programs for calculation of solar and thermal radiation in the Earth's atmosphere, see more details at http://www.libradtran.org/.

3.1. Synthetic SCEs due to the Variation in Atmospheric Transmission

We first generate a grid of atmospheric transmission curves for a range of airmass, barometric pressure, AOD, α, PWV, and Ozone using *libRadTran*. We then compute SCEs due to the variation in atmospheric transmission using Equation (9) by varying one atmospheric component at a time but keeping the fiducial instrumental throughput unchanged.

We calculate Δm when the airmass changes from $X = 1.2$ to $X = 1.8$. Figure 2 shows the ratio of atmospheric transmission at two different airmasses and Δm for O5V-M6V stars introduced by this airmass change, as a function of $g-i$ color. Δm due to the airmass change is more than ±10 mmag in the g band for O stars and M stars, and a few mmag in the u and r bands. Δm in the i, z, and Y bands is small. The SCEs due to the airmass change are essentially the "second-order extinction coefficient" or "airmass color extinction coefficient," which is known to increase toward bluer wavelengths (Henden & Kaitchuck 1990).

We run a similar calculation for the change in PWV from PWV = 3 mm to PWV = 10 mm and show the results in Figure 3. Δm due to the PWV change is mainly in the z and Y bands. The errors can be as large as $+10$ mmag in the z band and -4 mmag in the Y band, and thus an error of >10 mmag in $z-Y$ color. As mentioned earlier, molecular absorption does not vary linearly with column density, and therefore Δm caused by a PWV change from PWV = 3 mm to PWV = 10 mm is about the same as that from PWV = 0 to PWV = 3 mm or from PWV = 10 mm to PWV = 20 mm.

We also perform a similar calculation for Δm when barometric pressure, aerosol and ozone change in the atmosphere. We list Δm in Table 1 for an M6V star ($g-i\sim4$) as a summary for all above cases, after the gray-term has been removed using a G2V star. Δm caused by a change of the barometric pressure is very small. An extreme case of the barometric pressure change from 779 hpa to 789 hpa results in photometric errors of no more than 0.5 mmag in any band.

Δm caused by ozone variation is also small; an ozone change from 270 DU to 230 DU, which is an extreme case of the smallest ozone column density measured by the OMPS Nadir Mapper at the longitude and latitude of CTIO, results in $\Delta m < 1$ mmag in any band, and of only a few tenths of mmag in the g and r bands due to the Chappuis band. The DECam optics essentially has no throughput below 350 nm, so the ozone variation impact on u-band photometry is also negligible. This might not be the case for other cameras with greater response below 350 nm.

The change in aerosol optical depth affects mostly the g and r bands. As shown in Table 1, increasing $\rm AOD_{550}$ from 0.02 to 0.20 and keeping α unchanged results in $\Delta m = -11$ mmag in the g band. If the increase of the aerosol optical depth is due to the larger size of the aerosol particles, then α would decrease and Δm would be smaller compared to the unchanged α case. Equation (7) shows that an increase of AOD makes the atmospheric transmission spectrum redder and a decrease of α makes the transmission spectrum bluer. Therefore, larger particle size (i.e., smaller α) with larger AOD might introduce very small Δm in one or more bands. AOD and α are somewhat degenerate for the *shape* of the atmospheric transmission.

The synthetic SCEs in Table 1 are calculated when one of the atmospheric components changes from the fiducial while

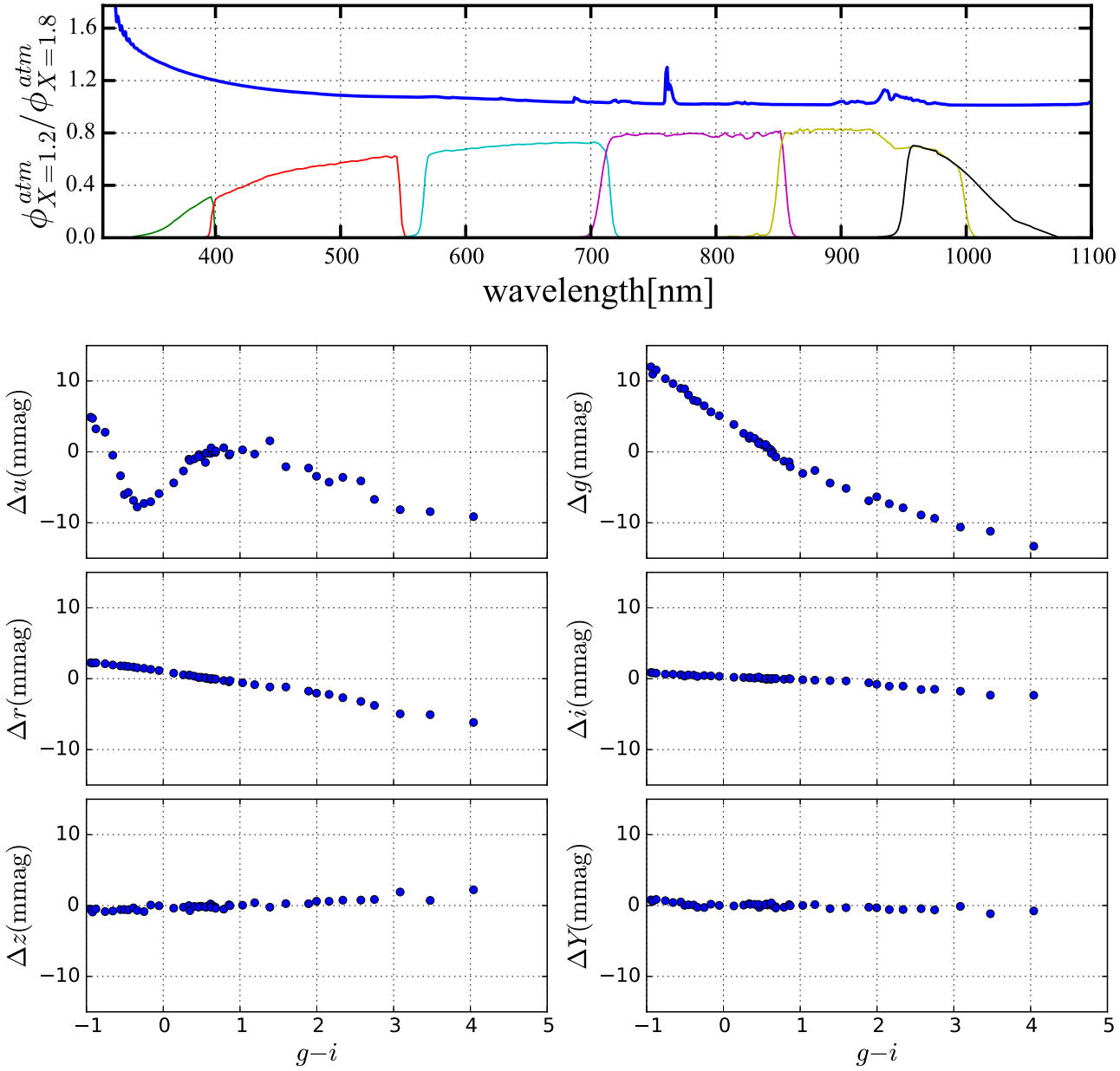

Figure 2. Top panel: the ratio of the atmospheric transmission for two airmass values, $X = 1.2$ and $X = 1.8$. The fiducial instrumental throughput $\phi^{\rm inst}_{\rm ref}(\lambda)$ for the *ugrizY* bands is also shown in the plot as reference. Bottom panels: synthetic SCEs in the *ugrizY* bands for O5V-M6V stars introduced by this airmass change, as a function of $g - i$ color.

the other components remain unchanged. Under some conditions, the SCEs can be significantly larger. For example, Δm for a PWV change from 3 mm to 10 mm will be much larger than 10 mmag if the airmass is at $X = 2.0$ instead of the fiducial $X = 1.2$. Of course, cumulative effects can also be larger.

In this section, we calculated the synthetic SCEs on stellar photometry caused by the variation in the atmospheric transmission. The SCEs caused by the variations in barometric pressure and ozone are very small. Variations in airmass and aerosol mainly affect the DES photometry in the *ugr* bands; variations in PWV mainly affect the DES photometry in the *zY* bands, as shown in Table 1. This is the primary reason that DES built and deployed aTmCam: to measure the PWV and aerosol at CTIO during DES operations. Furthermore, in order to provide a cross-check of the amount of PWV measured by aTmCam, DES has also installed a high-precision dual-band Global Positioning System (GPS). The GPS is used to measure the PWV, as the variation of PWV affects arrival time of the GPS signal via the increased index of refraction (Blake & Shaw 2011). The measured PWV by aTmCam and GPS agrees within the joint uncertainties of the two measurements. More details about a direct comparison can be found in (Li et al. 2014).

3.2. Synthetic SCEs due to the Variation in Instrumental Throughput

In this section, we study the synthetic SCEs, Δm, due to the variation in the instrumental throughput. For reference, SDSS discovered variations of the instrumental throughput over its survey period (Doi et al. 2010). Such variations could introduce

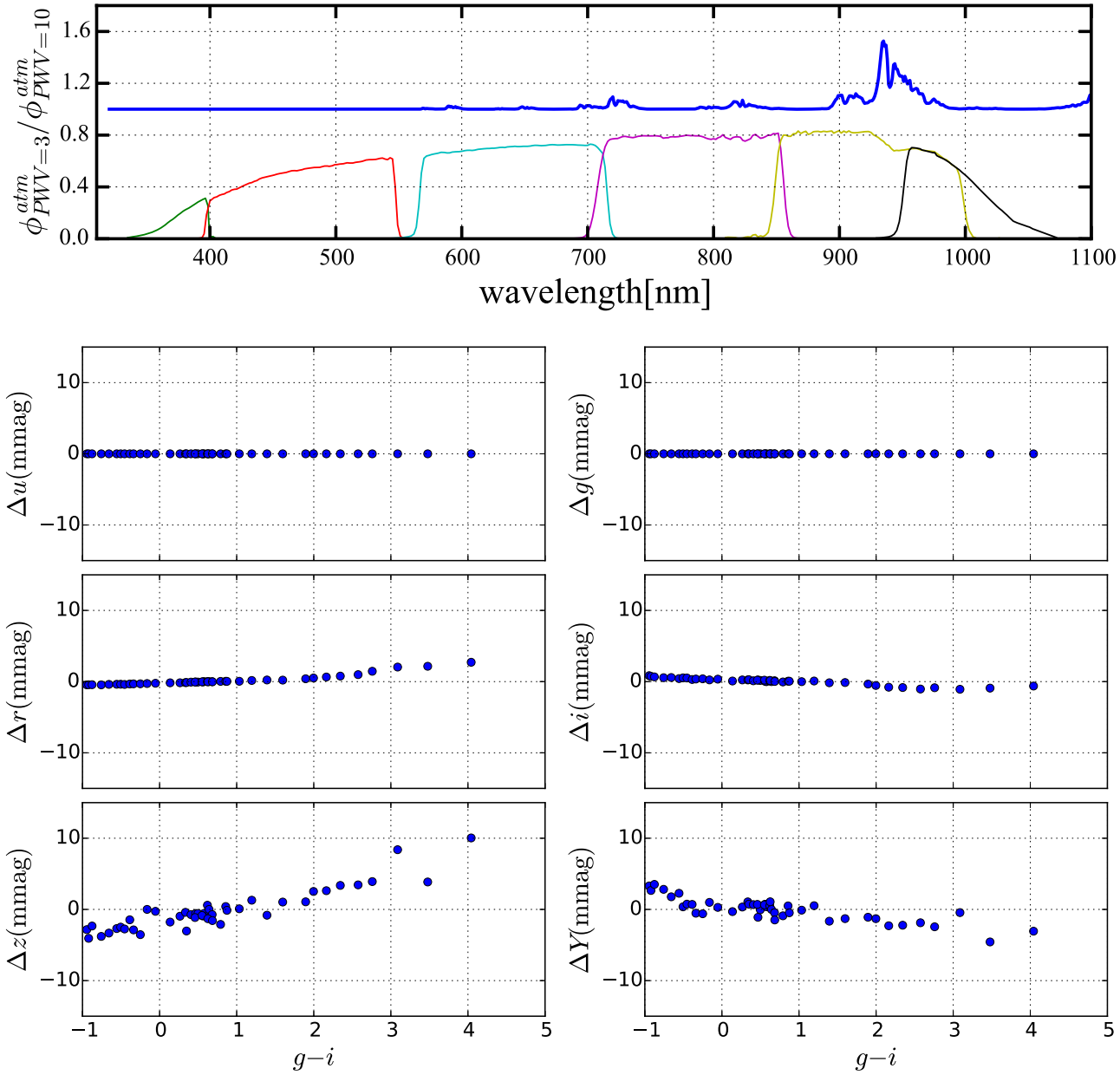

Figure 3. Top panel: the ratio of the atmospheric transmission for two PWV values, PWV = 3 mm and PWV = 10 mm. Bottom panels: synthetic SCEs in the *ugrizY* bands for O5V-M6V stars introduced by this PWV change, as a function of $g - i$ color.

SCEs similar to those caused by the variation in the atmospheric transmission. So far, DES has not seen a variation in instrumental throughput over time from the DECal scans in the past three years; however, data from DECal have shown a shift of either the blue or red edges of the filter bandpasses over the focal plane.

We shift the fiducial instrumental throughput $\phi^{\rm inst}_{\rm ref}(\lambda)$ 2 nm toward the longer wavelength and define it as a changed instrumental throughput $\phi^{\rm inst}(\lambda)$. We then calculate Δm due to this shift for O5V-M6V stars, shown in Figure 4 and Table 1. We again use a G2V star as reference to remove the gray term, as this is removed by the illumination correction using star-flats in the calibration procedure of DES. Except for the *u* band, the Δm in the other 5 bands are at the level of 1%–2%. The actual bandpass shifts from the DECal scans in *griz* bandpasses are roughly 1, 3, 6, and 2 nm, respectively, but only one of the bandpass edges shift, instead of both. The *u* and *Y* bands show almost no edge shift. More details about DECal and bandpass variations will be presented in J. L. Marshall et al. (2016, in preparation).

4. SCES IN STARS AS SEEN IN DES OBSERVATIONS

As noted earlier, DES obtains its data with the DECam camera on the Blanco 4 m telescope at CTIO. The data are transferred in near real-time over the course of each night to the National Center for Supercomputing Applications at the University of Illinois at Urbana-Champaign, where the DES Data Management team performs an initial nightly processing of the data, including image detrending, cataloging, and astrometric calibration of the individual exposures. There is also an annual re-processing, which includes a full re-processing of the single-epoch exposures, a global

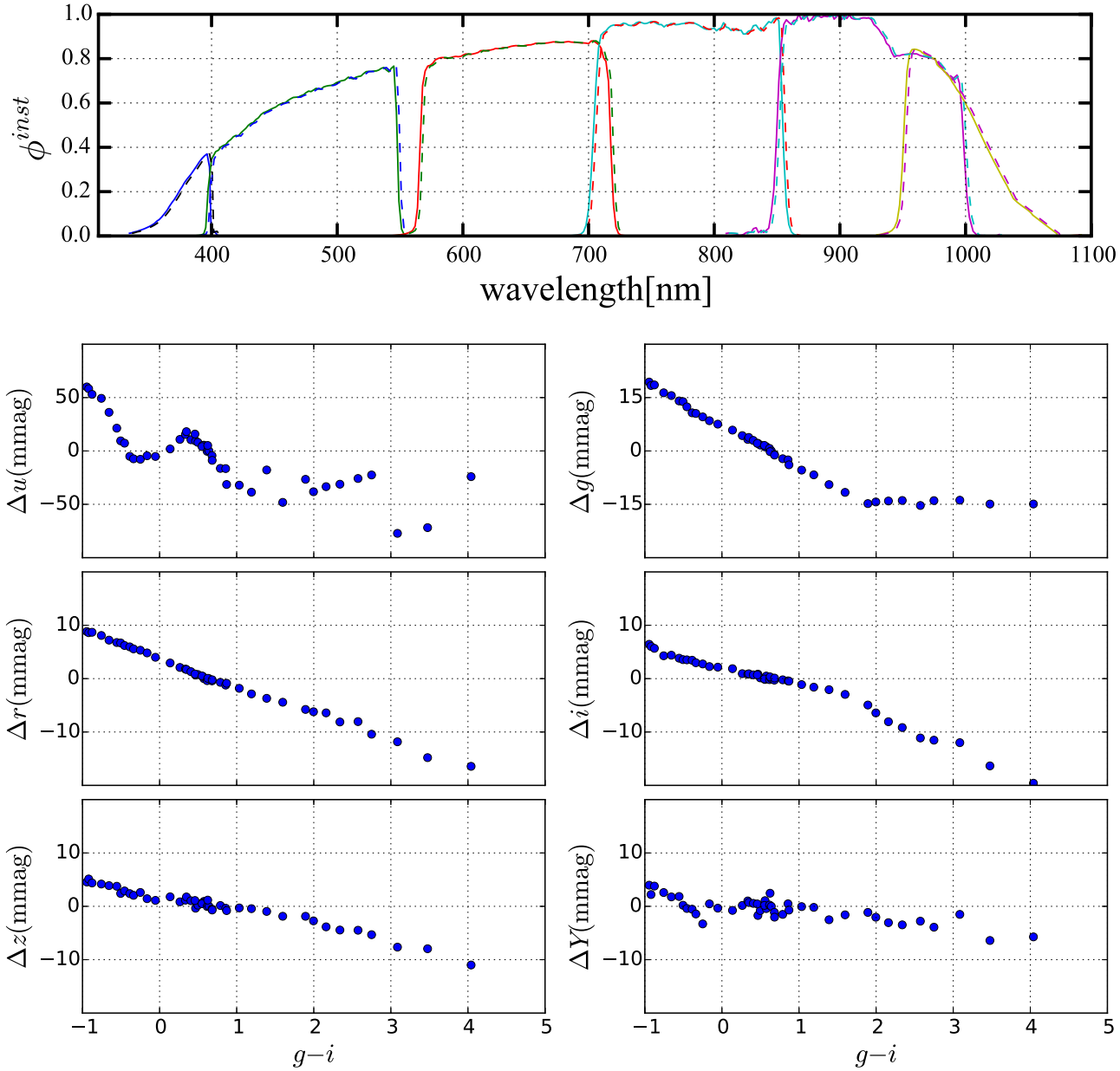

Figure 4. Top panel: solid lines are the fiducial instrumental throughput $\phi^{\rm inst}_{ref}(\lambda)$ for the *ugrizY* bands. Dashed lines are the instrumental throughput with a 2 nm shift toward the longer wavelength. Bottom panels: synthetic SCEs in the *ugrizY* bands for O5V-M6V stars introduced by this 2 nm bandpass shift, as a function of $g-i$ color. Note that the scales for the *u* and *g* bands are different from the other four bands.

photometric calibration of the data, and a coadd of overlapping exposures. An overview of the process is described in Balbinot et al. (2015), and details can be found in R. A. Gruendl et al. (2016, in preparation). The current global photometric calibration only considers the grayscale zeropoint correction, and therefore the SCEs have not been corrected in the current catalog. In order to show that SCEs exist in the catalog, we used the calibrated photometry derived using single epoch exposures from DES.

In this section, we give two examples using a test sample from DES data. We present the SCEs due to the PWV variation and due to the location on the DECam the focal plane. We show that SCEs in DES observations match synthetic SCEs to within a few mmag, which suggests that corrections based on measurements from the auxiliary calibration system (aTmCam + DECal) can be used to significantly improve photometric precision.

4.1. SCEs due to PWV Variation

We first show how the change of the PWV in the atmosphere affects the photometry in DES. The PWV was measured by aTmCam during DES observations.

Standard star fields are observed on every photometric night in the DES during evening and/or morning twilight. For one of DES standard star fields SDSSJ2300+0000 ($\sim$3 deg^2), Figure 5 shows the *z*-band stellar photometry difference, Δz, between two exposures taken on different nights, as a function of $g-i$ color of the stars. Δz is derived from the photometry in the single epoch catalog from the standard star calibration exposures. The position of the stars

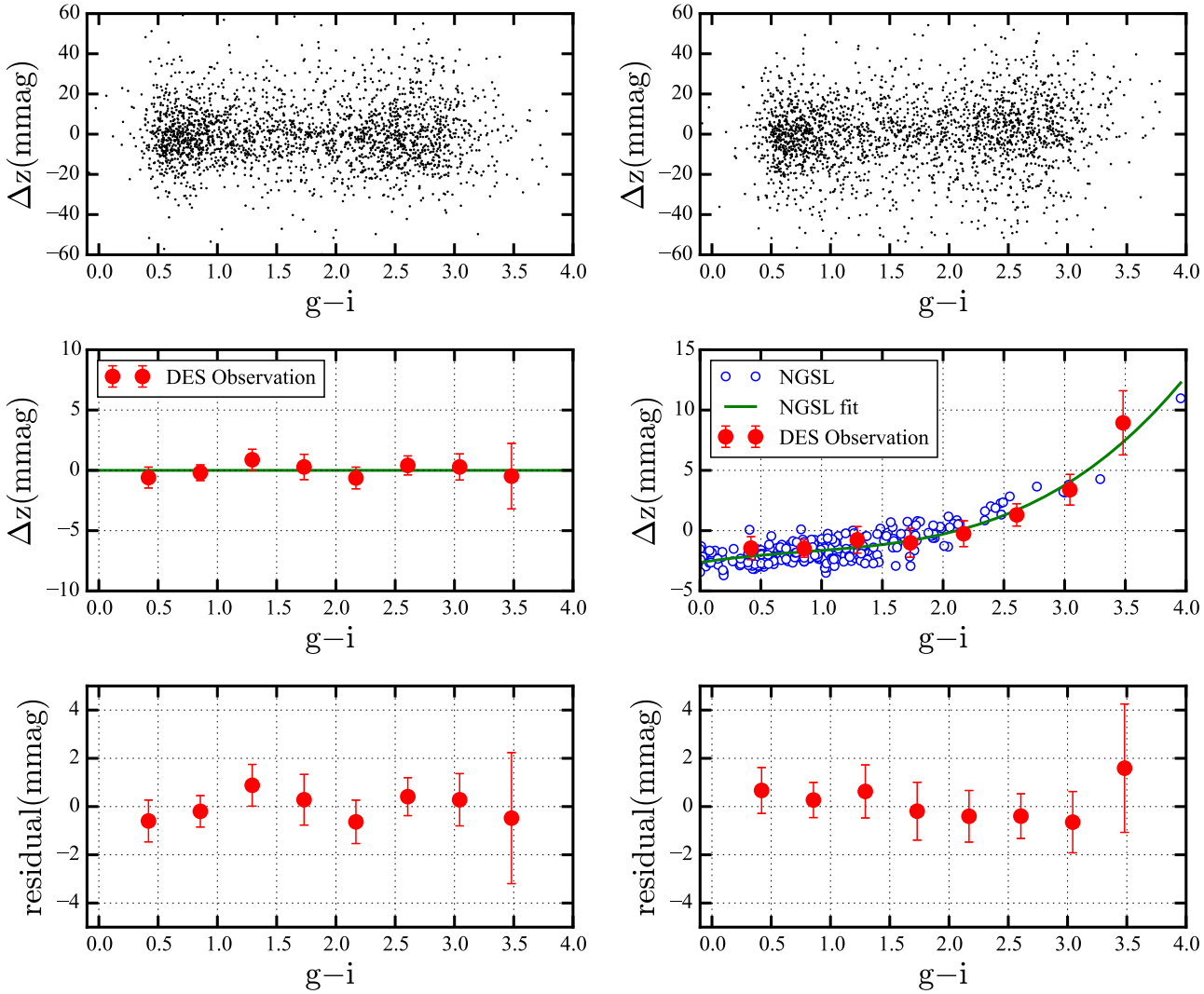

Figure 5. Measurements of the differences of z-band photometry, Δz, on two nights with similar PWV (left) and two nights with different PWV (right), as a function of the $g - i$ color of stars. Top panels: each black dot is a Δz from one star. Middle panels: stars with $0.2 < g - i < 3.7$ are divided into 8 bins and the average of Δz in each bin is calculated and shown as the red filled circles. The error bars show the error of the mean in each bin. A green line of $\Delta z = 0$ is shown on the left as the PWV is similar on those two nights. In the right panel, the green line is a third-order polynomial fit to the synthetic SCEs calculated using the atmospheric transmission models and the stellar templates, shown as the blue open circles. Bottom panels: residuals of the average of Δz in each bin, after corrections with the fit to the synthetic errors (i.e., green lines) in the middle panels.

on the CCD focal plane in two standard star exposures is constant to within the pointing error of the telescope (roughly 5 arcsec), so there are no significant SCEs from the variation of the instrumental throughput over the focal plane. The exposures are selected to be taken at the same airmass to ensure there are no SCEs from the airmass change. The selection criteria of $-0.002 < spread\_model\_i$[42] < 0.002 and $z < 18$ mag are applied in order to ensure that the targets are all bright stars so that the statistical errors from photon fluctuations are negligible (<5 mmag on average). We adopted the $g - i$ color for each star from the photometry in the coadd catalog. Since the coadd photometry is essentially the average over many exposures taken under different conditions, the $g - i$ color from coadd catalog is averaged over different SCEs and might be slightly different from the $g - i$ color from a single-epoch. However, this should not be a problem as such a color difference would be a second-order effect to the SCEs and should be negligible (i.e., <1 mmag).

We first calculate Δz for two exposures for nights 2014 November 13 and 2014 November 12, which has PWV = 3.6 mm and PWV = 4.2 mm from the measurements by aTmCam, shown in the top left panel of Figure 5; we then perform the same calculation on nights 2014 November 13 and 2014 November 15, which have PWV = 3.6 mm and PWV = 13.6 mm, shown on the top right panel. In both cases, there are more than 3000 stars matched from 2 exposures. There is an obvious trend in the top right panel showing that Δz is correlated with $g - i$ when there is a large difference between the PWV values.

We divide these stars into 8 equal-width bins over the range $0.2 < g - i < 3.7$. Except for the last bin, which only has about 60 stars, all bins have more than 300 stars. We calculate the average of Δz in each bin, shown as the red filled circles in the middle panels of Figure 5. The error bars show the error of

[42] Spread model is a parameter measured by SExtractor (Bertin & Arnouts 1996). It describes whether an object is better fit by the PSF or a broadened version of the PSF. It may be used as an indicator for star-galaxy separation (Desai et al. 2012).

the mean in each bin. On nights with similar PWV, the average of Δz is consistent with zero for all types of stars, as shown in the middle left panel. However, on the nights with a large difference in PWV, the average of Δz deviates from zero for red stars, as shown in the middle right panel. The most significant difference is at $g - i \sim 3.5$, where Δz is almost 4σ away from zero. This is strong evidence showing the existence of SCEs when the PWV changes.

We calculated the synthetic Δz when the atmospheric transmission changes from PWV = 3 mm to PWV = 13 mm. We followed the same steps as discussed in Section 3.1, except that instead of using a G2V star as the reference star, we used stars with $g - i \sim 2$ as reference stars to remove the gray-term variation, as stars with $g - i \sim 2$ tend to have zero errors in Δz between these two exposures. Furthermore, instead of using the Pickles Atlas, we used the stellar template from Next Generation Spectral Library[43] (NGSL), which contains flux calibrated stellar templates for more than 350 stars. We note that the synthetic SCEs calculated using NGSL and the Pickles Atlas generally show the same trend. As shown in Figure 3, the synthetic SCEs using the Pickles Atlas have a few millimag of scatter in the z and Y bands. We therefore adopted NGSL to compare with DES data as it contains a much larger sample of stellar templates. The synthetic SCEs calculated using each stellar template in NGSL are shown as open circles in the middle right panel of Figure 5.

We then fit a third-order polynomial to the computed synthetic Δz, and show this curve as a green line in middle right panel of Figure 5. The difference between the DES data and a fit to the synthetic SCEs using the NGSL templates are shown in the lower panels of Figure 5. The difference is less than 2 mmag over the $g - i$ color range. We emphasize that the fit is *NOT* to DES data, but rather it demonstrates that the SCEs due to the measured PWV change between the two nights are removed exceptionally well.

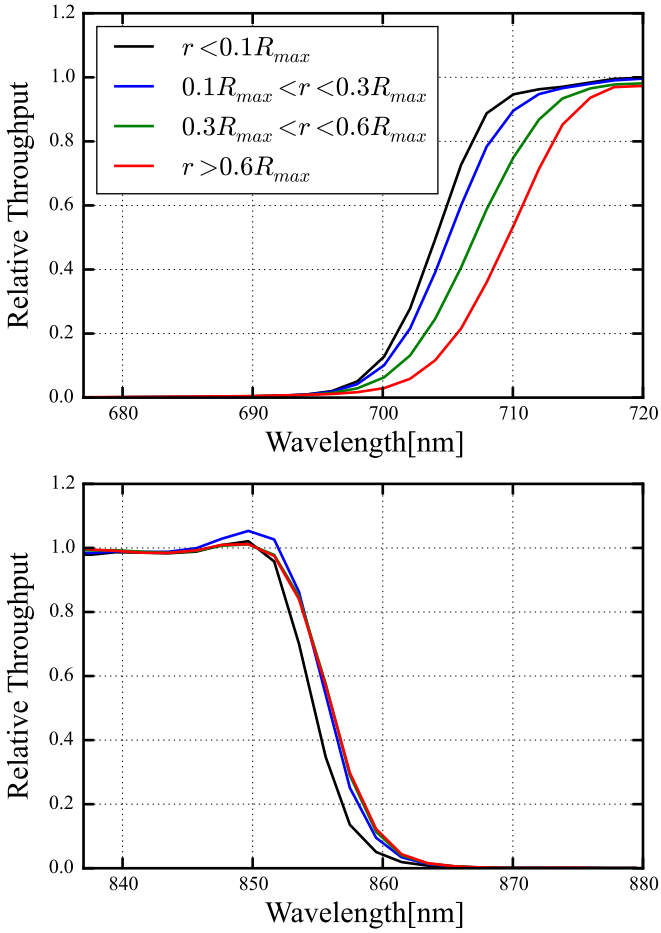

Figure 6. Relative throughput from a DECal scan around the cut-on (cut-off) wavelength in the top (bottom) panel from 4 Regions defined in the text. The throughput is normalized at 770 nm. Note there is about a 6 nm shift from the center of the focal plane to the edge of the focal plane.

4.2. SCEs Due to Location on the DECam Focal Plane

Here we show how the variation of instrumental throughput over the DECam focal plane affects the photometry in DES. We use the i band as the example since the i band has the largest bandpass edge shift measured from the results of DECal scans.

We divide the DECam focal plane into 4 regions based on the location of the center of the 62 CCD chips on the focal plane: Region 1 (0–0.1$R_{\rm max}$), Region 2 (0.1$R_{\rm max}$–0.3$R_{\rm max}$), Region 3 (0.3$R_{\rm max}$–0.6$R_{\rm max}$), and Region 4 (0.6$R_{\rm max}$–$R_{\rm max}$), where $R_{\rm max}$ is the maximum radius of the focal plane. The relative throughputs from DECal scans around the blue (red) edge are shown in the top (bottom) left panel of Figure 6. The average throughput in four different regions is normalized to the value at 770 nm. The figure shows that there is about a 6 nm shift at the blue edge when comparing the center of the focal plane to the edge of the focal plane.

We use the calibrated DES data in the same area as the standard star field SDSSJ2300+0000 to calculate the SCEs in the i band. We use the single epoch results from the survey exposures instead of the standard star calibration exposures. Since the tilings from the survey exposures have some small spatial offset (i.e., "dithered"), each star has been observed multiple times using different regions of the DECam focal plane. The same selection criteria as in Section 4.1 ($-0.002 < spread\_model < 0.002$ and $z < 18$ mag) are applied in order to ensure that the targets are all bright stars. We also make an airmass requirement ($1.12 < X < 1.22$) to ensure minimal SCEs from the change of airmass. We then determine the i-band magnitude in four regions as described above, i_1, i_2, i_3, and i_4 for Regions 1 to 4, respectively. For each star observed in Region 4, we find the same star in the other three regions when it is available and calculate the difference Δi. We found 291 matches for Regions 1 and 4; the differences $\Delta i_{14} = i_1 - i_4$ are calculated and shown in the top left panel of Figure 7. We bin the DES data in a similar way as in Section 4.1 and calculate the synthetic SCEs using the stellar spectra from NGSL, the instrumental throughputs for Regions 1 and 4 from the DECal scans and the fiducial atmospheric transmission model, shown in the middle left panel of Figure 7. A fourth-order polynomial fit to the synthetic SCEs is shown as the green line in the same panel. We repeat the calculation and show the Δi for Regions 2 and 4 and Regions 3 and 4 in the middle column and right column of Figure 7. There are 1890 matches for Regions 2 and 4 and 4189 matches for Regions 3 and 4, respectively. The bottom panels show the residuals of the binned Δi after correction using the fit from the synthetic SCEs calculation. We show here that Δi after

[43] https://archive.stsci.edu/prepds/stisngsl/

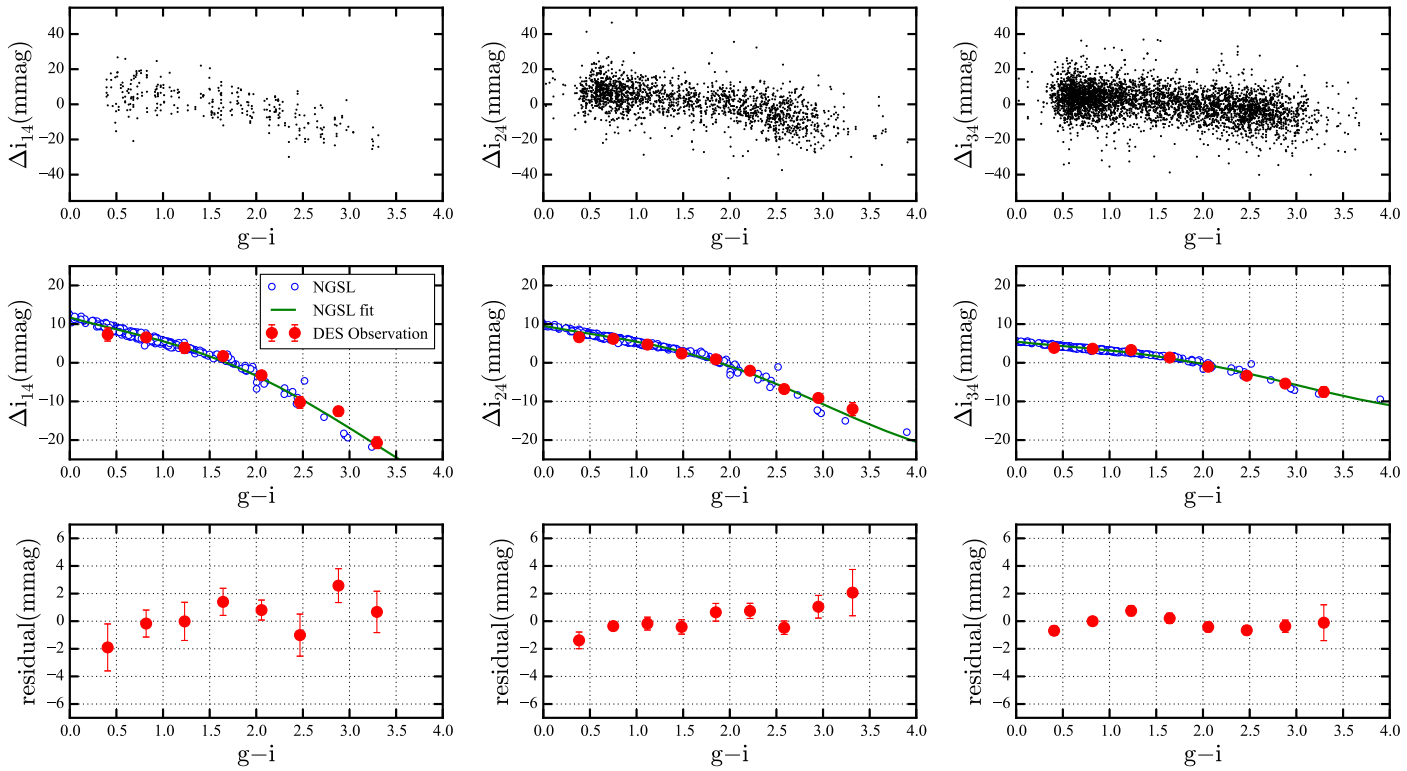

Figure 7. Top panels: Δi for Regions 1 and 4 (left), Regions 2 and 4 (middle), and Regions 3 and 4 (right), as a function of $g - i$ color. There are 291, 1890, and 4189 points in the left, middle, and right panels, respectively. Middle panels: we divided these stars into 8 bins and then calculated the average of Δi in each bin, shown as the red filled circles. The error bars show the error of the mean in each bin. Also calculated are the synthetic SCEs using the stellar spectra from NGSL, shown as the blue open circles. A fourth-order polynomial fit to the synthetic SCEs is shown as the green line. Bottom panels: residual plots of the binned Δi minus the fit from the synthetic SCEs. Note that the vertical scale for each panel is different.

Table 2
Residual Errors on a M6V Star ($g - i \sim 4$) when a Measurement by an Auxiliary Instrument has Small Uncertainties

			Synthetic Residual SCEs (mmag)					
Component	Measured	True	u	g	r	i	z	Y
Aerosol	$AOD_{550} = 0.02$, $\alpha = 1$	$AOD_{550} = 0.04$, $\alpha = 1$	−0.36	−1.3	−0.68	−0.41	−0.15	−0.02
	$AOD_{550} = 0.20$, $\alpha = 1$	$AOD_{550} = 0.20$, $\alpha = 0.9$	0.47	1.4	0.58	0.28	0.08	0.01
PWV	PWV = 3 mm	PWV = 3.3 mm	0	0	0.25	−0.05	0.92	−0.27
Instrument	DECal scan	shift 0.2 nm	−6.9	−1.5	−1.6	−1.9	−1.0	−0.74

the correction is less than <3 mmag for any stars at any position of the focal plane.

The SCEs due to position change are essentially the instrumental color-term over the DECam focal plane. It is usually calculated empirically using stars to get the correction to first order. Such empirical linear color corrections are good for stars with $0 < g - i < 2$. However, for very red stars and non-stellar objects, an empirical linear correction is not sufficient.

4.3. Residual Errors After Correction

Above we show that measurements of the atmospheric transmission and instrumental throughput can be used to correct imaging data to high photometric precision. Any system that determines the shape of the atmospheric transmission, however, will not produce perfect results and there will be errors in the determined values of the PWV, AOD, etc. Table 2 shows the effects of uncertainties in the determination of the important parameters. Notably, measurements of the PWV that are accurate to ∼10% generally are adequate to ensure that residual errors after correction are less than 1 mmag in all DECam bands. Similarly, AOD and α determinations accurate to 0.02 and 0.1 also generally produce corrections that give less than ∼1 mmag residual errors.

Measurement of the variation in instrumental throughput across the focal plane generally require determination of the wavelengths of any shift in the bandpass to ∼0.2 nm precision. Determination of the bandpass to this level will give <2 mmag residual error in most bands.

5. SYNTHETIC SCES ON NON-STELLAR OBJECTS

Since the SED of a non-stellar object is significantly different from that of a star, the SCEs on some of the non-stellar objects can be larger than what we have seen for stars. We show two examples in this section: SNe Ia and elliptical galaxies. We calculate the synthetic SCEs Δm for these two

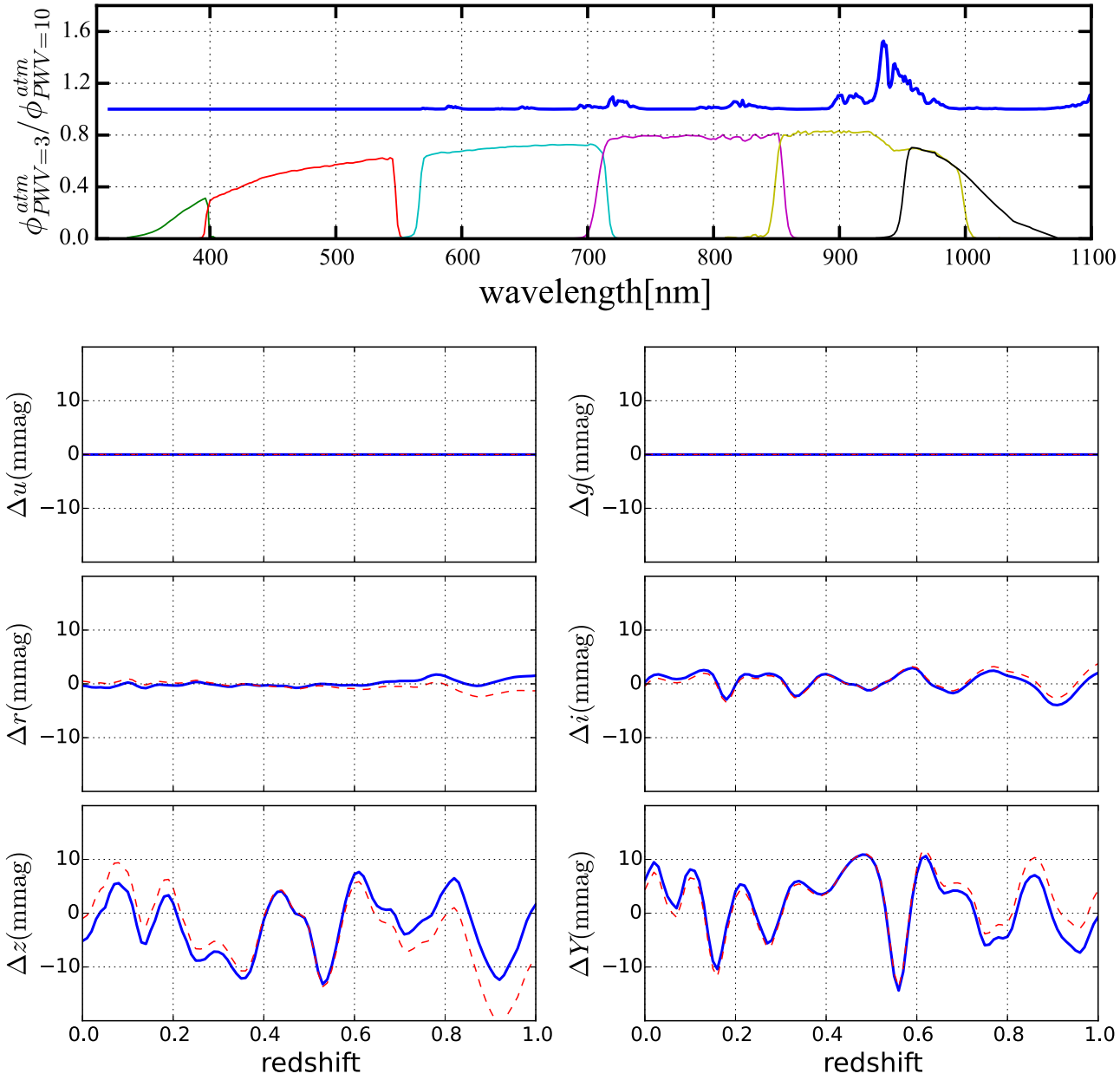

Figure 8. Synthetic SCEs in the *ugrizY* bands for SNe Ia as a function of redshift when the PWV in the atmosphere changes from 3 mm to 10 mm, shown as the blue sold lines. The red dashed lines are the residual errors after using the correction derived for stars with the same $g - i$ color as the SNe Ia.

types of objects using Equation (9). As the shape of the SEDs changes with redshift, the Δm are also redshift dependent.

5.1. Type Ia Supernovae

For the DES survey, the sub-percent photometry precision goal comes from supernova cosmology, which needs precise photometry so that one can measure the luminosity distances of SNe Ia over a wide redshift range.

Here, we give an example of how the synthetic SCEs change with redshift. Figure 8 shows Δm caused by a PWV change from 3 to 10 mm for a SN Ia as a function of redshift z. We use the SED from SN2011fe (Pereira et al. 2013) as the template for the calculation. The template was taken 0.27 days prior to maximum brightness. The peak-to-valley errors can be as large as 20 mmag for the z and Y bands over redshift $z = 0$ to $z = 1$, shown as the blue solid lines. Because a SN Ia SED is very different from that of a star, the SCEs for a star and a SN Ia are very different, even if they share the same $g - i$ color. The red dashed lines in Figure 8 show the SCEs residuals after naively using the corrections derived from stars with the same $g - i$ color as the SNe Ia, i.e., synthetic SCEs calculated in Section 3.1. As the figure shows, the SCEs are not properly corrected, and sometimes are even larger.

In Table 3, we summarize the synthetic SCEs on SNe Ia by the changes of other atmospheric components or by a 2 nm shift. It is similar to Table 1 except that the SCEs here are calculated as the peak-to-valley SCEs over redshift $z = 0$ to $z = 1$.

5.2. Galaxies

Precise photometry helps the determination of photometric redshifts of galaxies (Wolf et al. 2001; Ilbert et al.

Table 3
Peak-to-valley SCEs on SNe Ia Over Redshift $z = 0$ to $z = 1$

Component	Fiducial	Changed	Synthetic SCEs (mmag)					
			u	g	r	i	z	Y
Pressure	$P_0 = 779$ hpa	$P_0 = 789$ hpa	0.8	0.9	0.1	0.2	0.1	0.1
Aerosol	$AOD_{550} = 0.02$, $\alpha = 1$	$AOD_{550} = 0.20$, $\alpha = 1$	11	26	7	4	2	1
	$AOD_{550} = 0.02$, $\alpha = 1$	$AOD_{550} = 0.20$, $\alpha = 0.5$	4	11	3	2	1	0.7
PWV	PWV = 3 mm	PWV = 10 mm	0	0	3	7	20	27
Ozone	Ozone = 270 DU	Ozone = 230 DU	0.04	1.7	1	0.1	0	0
Airmass	$X = 1.2$	$X = 1.8$	31	30	7	4	6	7
Instrument	DECal scan	shift 2 nm	186	99	33	22	19	28

Table 4
Peak-to-Valley SCEs on Elliptical Galaxies Over Redshift $z = 0$ to $z = 2$

Component	Fiducial	Changed	Synthetic SCEs (mmag)					
			u	g	r	i	z	Y
Pressure	$P_0 = 779$ hpa	$P_0 = 789$ hpa	0.6	0.6	0.07	0.1	0.04	0.03
Aerosol	$AOD_{550} = 0.02$, $\alpha = 1$	$AOD_{550} = 0.20$, $\alpha = 1$	7	18	10	4	3	1
	$AOD_{550} = 0.02$, $\alpha = 1$	$AOD_{550} = 0.20$, $\alpha = 0.5$	3	7	5	2	2	0.7
PWV	PWV = 3 mm	PWV = 10 mm	0	0	4	4	26	20
Ozone	Ozone = 270 DU	Ozone = 230 DU	0.03	1.2	1.6	0.1	0	0
Airmass	$X = 1.2$	$X = 1.8$	26	21	11	4	7	6
Instrument	DECal scan	shift 2 nm	79	36	28	26	17	22

2006). We therefore study the synthetic SCEs for galaxies. We used a spectral template of elliptical galaxies from Coleman et al. (1980) for this calculation. We summarize the peak-to-valley SCEs on elliptical galaxies over redshift $z = 0$ to $z = 2$ in Table 4. As an example, Figure 9 shows Δm caused by a 2 nm shift of the instrumental throughput toward longer wavelength, as a function of redshift. The drop of Δr around redshift $z = 0.4$, Δi around redshift $z = 0.8$, Δz around redshift $z = 1.1$, and ΔY around redshift $z = 1.3$ are due to the 4000 Å break. We again use the correction derived from stars with the same $g - i$ and the SCEs residuals after correction are shown as red dashed lines in the same figure.

Similar to SNe Ia, the SCEs are not properly corrected since the galaxy SED is different from that of a star. However, it is worth noting that the star-derived corrections using $g - i$ color actually slightly correct the SCEs on galaxies. For example, in the *griz* bands, the red lines (after correction) are much closer to zero compared to the blue lines (before correction) for redshift $z < 1$. Here, we derive the corrections based on a fixed color $g - i$. This might be good enough for regular stars, as they form a well-defined stellar locus on a color–color diagram. We pick $g - i$ throughout the paper since $g - i$ ranging from -1 to 4 separates the blue stars from red stars.[44] However, $g - i$ might not be the best choice for SNe Ia and galaxies. Choosing a color close to the band of interest, e.g., $g - r$ for the g band, and $z - Y$ for the z band and/or Y band, or choosing a combination of multiple colors, might be better for these non-stellar objects. We leave further discussion of this to future work.

[44] For example, $g - r$ is not a good color to pick for red stars since all K and M stars tend to clump around $g - r \sim 1.5$. Therefore, it is hard to correct the SCEs on red stars using $g - r$ color.

6. SCES IN GROUND-BASED TRANSIT OBSERVATIONS

We discussed the SCEs in this paper mainly for the large area sky surveys like DES. However, the SCEs calculated here are not only limited to photometric calibrations in large surveys. The synthetic calculations presented in Table 1 can also be applied to any ground-based differential photometric measurements, such as exoplanet transients and other variable star measurements. For example, if the planet host is an M6V star and most of the reference stars in the field are G2V stars, then PWV varying from 3 mm to 10 mm can affect the photometry in the z band to ~1%. This is comparable to or even larger than the signal from a super-Earth transiting an M star. Similarly, variations in either the atmospheric transmission or instrumental throughput can also affect such measurements in other bands. If we correct the SCEs in these differential measurements with auxiliary systems, it is possible to improve the detection of Earth-like exoplanets around M star hosts in some ground-based transit observations such as the MEarth Project (Irwin et al. 2009; Berta-Thompson et al. 2015).

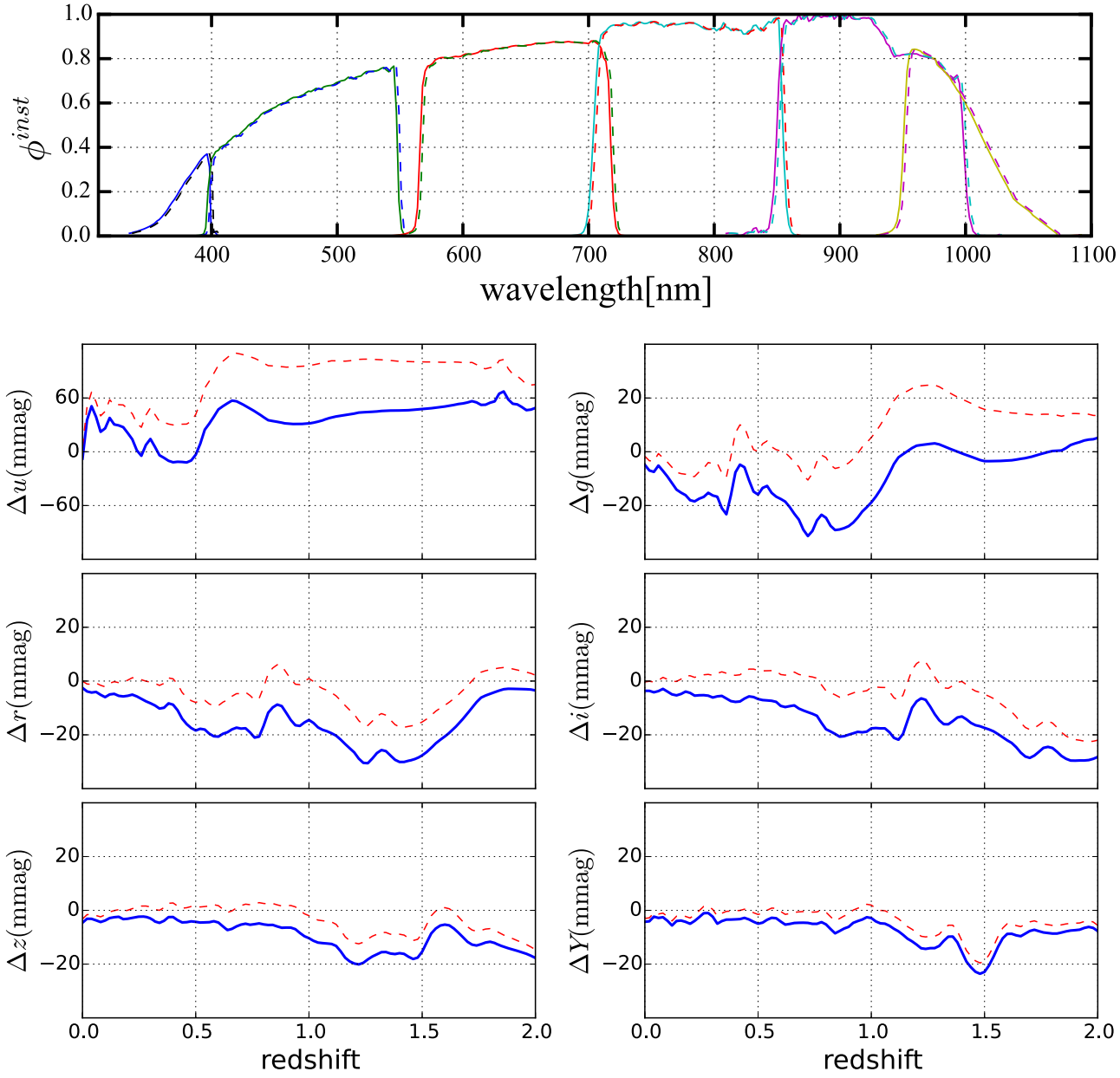

Figure 9. Synthetic SCEs in the *ugrizY* bands for elliptical galaxies as a function of redshift, when the instrumental throughput is moved by 2 nm toward longer wavelength. The red dashed lines show the residual errors after using the correction derived for stars with the same $g - i$ color as the elliptical galaxies. Note that the scale for the u band is different from the other five bands.

7. CONCLUSIONS

In this paper, we have demonstrated that the variation of the atmospheric transmission and the instrumental throughput introduce SCEs that depend on the color of the source object. We assess such SCEs for the DES as an example.

1. For stars, the SCEs caused by the change of airmass in each exposure and the change of PWV and aerosol in the atmosphere can be larger than 1%.
2. The SCEs caused by the change of the barometric pressure and ozone are smaller than 0.1% (or 1 mmag).
3. The SCEs caused by the bandpass edge shift over the detector focal plane can be as large as a few percent.
4. The SCEs can be corrected to 2–3 mmag or better if the shape of the atmospheric transmission and the instrumental throughput are well measured by auxiliary calibration system such as aTmCam and DECal.
5. For supernovae and galaxies, these SCEs are expected to be larger and also redshift-dependent. Figures 8 and 9 give examples of how SCEs change as a function of redshift for SNe Ia and elliptical galaxies.
6. For stars, we could derive a color term to first order and approximately correct the SCEs. However, such linear stellar color terms are not sufficient for getting color corrections for extremely red stars, SNe, and galaxies.

From this study, we suggest that, for large imaging surveys such as DES and LSST, one should first define a natural system response that represents the average condition of the survey, and also define a stellar SED as the reference SED that represents the average color of the calibration stars in the

survey. Then for each stellar object, one could calculate the synthetic SCEs using the stellar SED library together with the stellar color, as described in this paper, and use the synthetic SCEs as the corrections. For non-stellar objects like SNe Ia or galaxies, the redshifted SED need to be given as an input to derive such corrections.

Even though SCEs are systematic errors for each exposure, they will eventually introduce additional scatter on the final coadd photometry and affect the photometric precision of the surveys with multiple visits. This is true because: (1) the atmospheric transmission varies over a wide range of conditions and each exposure is likely to be taken with a different condition; (2) each exposure in the survey has a slight offset for multiple tilings so that the same object does not fall on the same location on the focal plane. Averaging over different conditions and different focal plane positions can reduce the amount of SCEs in the final coadd photometry. Exceptions include supernovae and other transients, for which there is only one measurement in a particular epoch.

This paper has gone through internal review by the DES collaboration. We thank the anonymous referee for comments and suggestions that improved the paper. T.S.L. thanks Michael Smitka, Nicholas Sunzeff, Željko Ivezić and Abhijit Saha for very helpful conversations. Texas A & M University thanks Charles R. '62 and Judith G. Munnerlyn, George P. '40 and Cynthia Woods Mitchell, and their families for support of astronomical instrumentation activities in the Department of Physics and Astronomy.

Funding for the DES Projects has been provided by the U.S. Department of Energy, the U.S. National Science Foundation, the Ministry of Science and Education of Spain, the Science and Technology Facilities Council of the United Kingdom, the Higher Education Funding Council for England, the National Center for Supercomputing Applications at the University of Illinois at Urbana-Champaign, the Kavli Institute of Cosmological Physics at the University of Chicago, the Center for Cosmology and Astro-Particle Physics at the Ohio State University, the Mitchell Institute for Fundamental Physics and Astronomy at Texas A&M University, Financiadora de Estudos e Projetos, Fundação Carlos Chagas Filho de Amparo à Pesquisa do Estado do Rio de Janeiro, Conselho Nacional de Desenvolvimento Científico e Tecnológico and the Ministério da Ciência, Tecnologia e Inovação, the Deutsche Forschungsgemeinschaft and the Collaborating Institutions in the Dark Energy Survey. The DES data management system is supported by the National Science Foundation under Grant Number AST-1138766. The DES participants from Spanish institutions are partially supported by MINECO under grants AYA2012-39559, ESP2013-48274, FPA2013-47986, and Centro de Excelencia Severo Ochoa SEV-2012-0234, some of which include ERDF funds from the European Union.

The Collaborating Institutions are Argonne National Laboratory, the University of California at Santa Cruz, the University of Cambridge, Centro de Investigaciones Enérgeticas, Medioambientales y Tecnológicas-Madrid, the University of Chicago, University College London, the DES-Brazil Consortium, the University of Edinburgh, the Eidgenössische Technische Hochschule (ETH) Zürich, Fermi National Accelerator Laboratory, the University of Illinois at Urbana-Champaign, the Institut de Ciències de l'Espai (IEEC/CSIC), the Institut de Física d'Altes Energies, Lawrence Berkeley National Laboratory, the Ludwig-Maximilians Universität München and the associated Excellence Cluster universe, the University of Michigan, the National Optical Astronomy Observatory, the University of Nottingham, The Ohio State University, the University of Pennsylvania, the University of Portsmouth, SLAC National Accelerator Laboratory, Stanford University, the University of Sussex, and Texas A&M University.

REFERENCES

Ångström, A. 1924, QJRMS, 50, 121125
Balbinot, E., Santiago, B. X., Girardi, L., et al. 2015, MNRAS, 449, 1129
Berta-Thompson, Z. K., Irwin, J., Charbonneau, D., et al. 2015, Natur, 527, 204
Bertin, E., & Arnouts, S. 1996, A&AS, 117, 393
Bessell, M., & Murphy, S. 2012, PASP, 124, 140
Bessell, M. S. 1990, PASP, 102, 1181
Betoule, M., Marriner, J., Regnault, N., et al. 2013, A&A, 552, A124
Blake, C. H., & Shaw, M. M. 2011, PASP, 123, 1302
Burke, D. L., Axelrod, T., Blondin, S., et al. 2010, ApJ, 720, 811
Burke, D. L., Saha, A., Claver, J., et al. 2014, AJ, 147, 19
Coleman, G. D., Wu, C.-C., & Weedman, D. W. 1980, ApJS, 43, 393
Deng, L.-C., Newberg, H. J., Liu, C., et al. 2012, RAA, 12, 735
Desai, S., Armstrong, R., Mohr, J. J., et al. 2012, ApJ, 757, 83
Doi, M., Tanaka, M., Fukugita, M., et al. 2010, AJ, 139, 1628
Flaugher, B., Diehl, H. T., Honscheid, K., et al. 2015, AJ, 150, 150
Glazebrook, K., Peacock, J. A., Collins, C. A., & Miller, L. 1994, MNRAS, 266, 65
Hansen, J. E., & Travis, L. D. 1974, SSRv, 16, 527
Henden, A. A., & Kaitchuck, R. H. 1990, Astronomical photometry : A Text and Handbook for the Advanced Amateur and Professional Astronomer (Richmond, VA: Willmann-Bell, Inc.)
High, F. W., Stubbs, C. W., Rest, A., Stalder, B., & Challis, P. 2009, AJ, 138, 110
Holberg, J. B., & Bergeron, P. 2006, AJ, 132, 1221
Ilbert, O., Arnouts, S., McCracken, H. J., et al. 2006, A&A, 457, 841
Irwin, J., Charbonneau, D., Nutzman, P., & Falco, E. 2009, in AIP Conf. Ser. 1094, 15th Cambridge Workshop on Cool Stars, Stellar Systems, and the Sun, ed. E. Stempels (Melville, NY: AIP), 445
Ivezić, Ž, Lupton, R. H., Schlegel, D., et al. 2004, AN, 325, 583
Ivezić, Ž, Smith, J. A., Miknaitis, G., et al. 2007, AJ, 134, 973
Landolt, A. U. 1992, AJ, 104, 340
Li, T., DePoy, D. L., Kessler, R., et al. 2012, Proc. SPIE, 8446, 2
Li, T., DePoy, D. L., Marshall, J. L., et al. 2014, Proc. SPIE, 9147, 6
LSST Science Collaboration, Abell, P. A., Allison, J., et al. 2009, arXiv:0912.0201
MacDonald, E. C., Allen, P., Dalton, G., et al. 2004, MNRAS, 352, 1255
Manfroid, J. 1995, A&AS, 113, 587
Mayer, B., & Kylling, A. 2005, ACP, 5, 1855
Padmanabhan, N., Schlegel, D. J., Finkbeiner, D. P., et al. 2008, ApJ, 674, 1217
Pereira, R., Thomas, R. C., Aldering, G., et al. 2013, A&A, 554, A27
Pickles, A. J. 1998, PASP, 110, 863
Querel, R. R., & Kerber, F. 2014, Proc. SPIE, 9147, 92
Rayleigh, L. 1899, PMag, 47, 375
Regnault, N., Conley, A., Guy, J., et al. 2009, A&A, 506, 999
Rheault, J.-P., DePoy, D. L., Marshall, J. L., et al. 2012, Proc. SPIE, 8446, 84466M
Schlafly, E. F., Finkbeiner, D. P., Jurić, M., et al. 2012, ApJ, 756, 158
Schuster, G. L., Dubovik, O., & Holben, B. N. 2006, JGRD, 111, D07207
Scolnic, D., Casertano, S., Riess, A., et al. 2015, ApJ, 815, 117
Stetson, P. B. 2000, PASP, 112, 925
Stetson, P. B. 2005, PASP, 117, 563
Stubbs, C. W., High, F. W., George, M. R., et al. 2007, PASP, 119, 1163
Stubbs, C. W., & Tonry, J. L. 2006, ApJ, 646, 1436
Tucker, D. L., Annis, J. T., Lin, H., et al. 2007, in ASP Conf. Ser. 364, The Future of Photometric, Spectrophotometric and Polarimetric Standardization , ed. C. Sterken (San Francisco, CA: ASP), 187
Wittman, D., Ryan, R., & Thorman, P. 2012, MNRAS, 421, 2251
Wolf, C., Meisenheimer, K., & Röser, H.-J. 2001, A&A, 365, 660
Yuan, H., Liu, X., Xiang, M., et al. 2015, ApJ, 799, 133